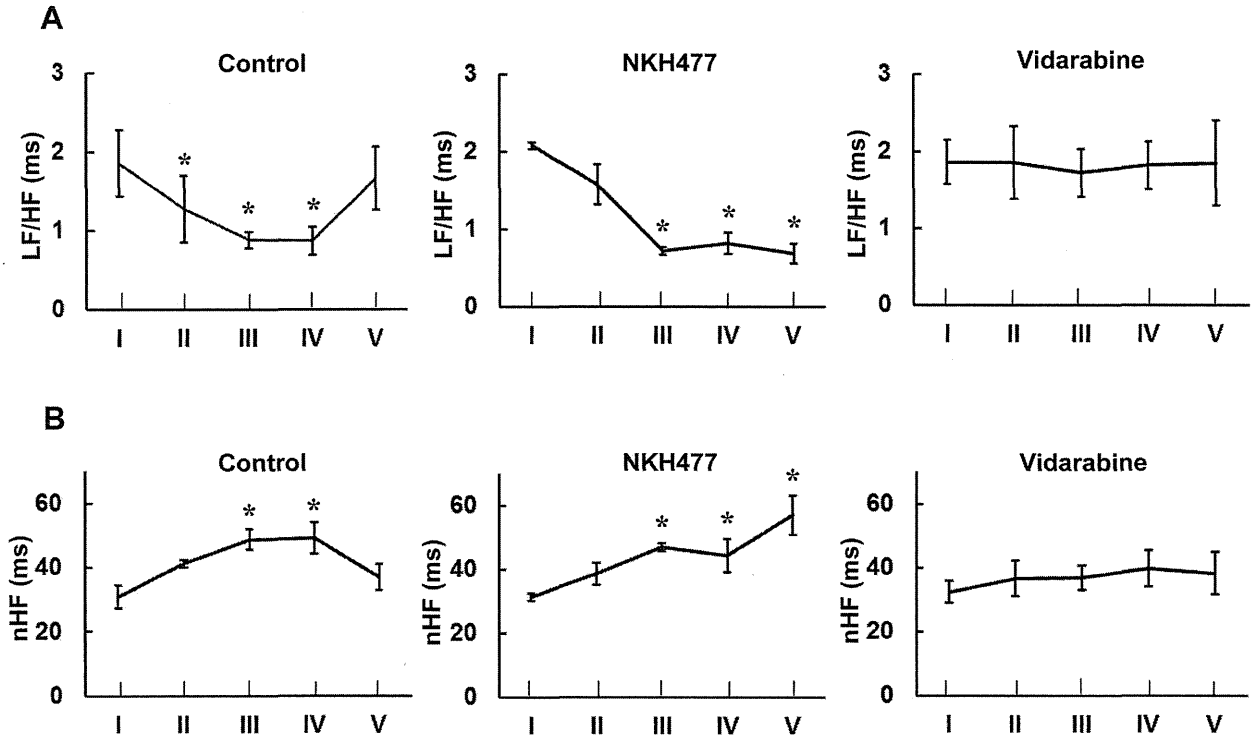

Fig. 8. Comparison of LF/HF and nHF during parabolic flights. A) LF/HF was compared as an index of sympathetic nerve activity in each phase during the first parabola in the control (n = 10), NKH477 (n = 7), and vidarabine (n = 8) groups (*$P < 0.05$ vs. phase I). B) nHF was compared as an index of parasympathetic nerve activity in each phase during the first parabola in control (n = 10), NKH477 (n = 7), and vidarabine (n = 8) groups (*$P < 0.05$ vs. phase I).

sent in the vidarabine group.

Effect of parabolic flight on nHF of HRV

HF power was normalized to account for differences in TP and was examined as an index of parasympathetic tone (16). When nHF was compared between normogravity (phase I) and microgravity (phase III), we found that it was significantly increased in microgravity in both the control and NKH477 groups (Fig. 8B) [control group (n = 10): phase I vs. phase III: 31 ± 3.6 vs. 49 ± 3.2 ms, $P < 0.05$; NKH477 group (n = 7): phase I vs. phase III: 31 ± 1.2 vs. 47 ± 1.2 ms, $P < 0.05$), suggesting that parasympathetic nerve tone was increased under microgravity in both the control and NKH477 groups. In contrast, there was no increase in nHF in the vidarabine group under microgravity (phase I vs. phase III: 32 ± 3.5 vs. 37 ± 3.8 ms, P = NS, n = 8), suggesting that microgravity-induced enhancement of parasympathetic nerve tone was attenuated in the vidarabine group.

Under hypergravity (phase IV), nHF showed a similar tendency to that under microgravity in the three groups.

nHF in post-microgravity (phase V) was returned to a similar level to that in pre-microgravity (phase I) in WT (37 ± 4.1 ms, P = NS), while it further increased in the NKH477 group (57 ± 6.2 ms, $P < 0.05$) (Fig. 8B). However, there were no such increases or decreases in the vidarabine group (38 ± 6.6 ms, P = NS).

Thus, parasympathetic nervous tone was transiently elevated in the control group, remained elevated in the NKH477 group, and showed no changes in the vidarabine group.

Taking these results together, in comparison to the control group, the NKH477 group showed continuous responses in the above autonomic (sympathetic and parasympathetic) parameters while the vidarabine group showed attenuated responses under micro- and hypergravity.

Discussion

Our current study demonstrated that activation of AC5 activity with NKH477 could stabilize HRV, while inhibition of AC5 with vidarabine could destabilize HRV under micro- and hypergravity during parabolic flight. Further, the absolute value of the total autonomic variability index (SDNN) was much greater in the vidarabine group than that in the control or NKH477 groups under microgravity as well as hypergravity. A marker of the sympathetic

nervous tone (LF/HF) was decreased to a greater degree in the NKH477 group relative to the control group, and a marker of parasympathetic tone (nHF) was instead increased to a greater degree in the NKH477 group; these changes were absent in the vidarabine group, indicating that pharmacological modulation of AC5 activity might be able to regulate the autonomic control of the heart rate under gravitational stress during parabolic flight.

AC consists of 9 mammalian transmembrane isoforms that differ in tissue distribution (3, 5), with type 6 AC (AC6) being the major fetal cardiac AC isoform, and AC5, the major cardiac isoform in adults (27, 28). All isoforms are stimulated by Gs, but AC5 and AC6 are the only Gi- and Ca^{2+}-inhibitable AC isoforms (3, 5). AC5 is responsible for at least one-third of the cardiac AC catalytic activity and plays an important role not only in sympathetic, but also parasympathetic cardiac function and heart rate without affecting Gi-gated K^+-channel current, which regulates normal pacing activity, as shown recently by us and others in AC5KO (7, 29). Overexpressing AC6 results in maintained basal HR (30), while overexpressing AC5 results in increased basal HR (13, 31), suggesting that AC5 may play an important role in regulating HR through the parasympathetic arm of the autonomic nervous system, as well as the sympathetic arm.

For many years, it has been recognized that many astronauts suffer from symptoms suggestive of autonomic dysfunction such as nausea, vomiting, and dizziness during the early days of space missions and their cardiovascular system subsequently adapts to the microgravity environment of space appropriately and effectively. However, on return to earth, from one-quarter to two-thirds of them have reduced orthostatic tolerance for a few weeks. The underlying molecular mechanisms remain unknown and are probably multifactorial, although alterations in the autonomic nervous system and/or neuromuscular function after spaceflight probably contribute to this problem (18, 19).

We have previously demonstrated that AC5 plays an important role in stabilizing HRV under microgravity, as well as hypergravity, during parabolic flight using genetically engineered mouse models (13). This present study has demonstrated that pharmacological activation/inhibition of AC5 activity can stabilize/destabilize the HRV not only under microgravity but also under hypergravity during parabolic flight. Importantly, NKH477 which was used in this study as a selective AC5 activator (NKH477) has been widely used for the treatment of acute heart failure in Japan since 1999. We will not need to wait for many years to get authorization for the use of NKH477 to treat autonomic dysfunction during and after space flight, if its usefulness is sufficiently confirmed by further studies.

There are plans for suborbital spaceflight or lunar tours for normal subjects as tourists, and also for prolonged space flight to Mars. It is also likely that not only astronauts, but also normal subjects will stay for up to several months in the international space station. Therefore, it is important to clarify the mechanism of the alterations in the autonomic nervous system and to develop suitable treatment. Our studies indicate that short-term, not long-term, pharmacological activation/inhibition of AC5 activity with NKH477 or vidarabine might rescue the autonomic dysfunction in the heart under microgravity in space and on earth after space flight, especially for untrained normal subjects.

Acknowledgments

This study was supported in part by grants from the Ministry of Health, Labor, and Welfare (Y.I.); the Kitsuen Kagaku Research Foundation (Y.I.); the Japanese Ministry of Education, Culture, Sports, Science, and Technology (Y.I., S.O., M.S., U.Y., R.K., Y.B., T.T., T.F.,Y.I.); Grant-in-Aid for Scientific Research on Innovative Areas (Y.I.); the Japan Space Forum (Y.I.); Takeda Science Foundation (Y.I., S.O., U.Y., M.S.); Yokohama Foundation for Advancement of Medical Science (S.O., U.Y., M.S., T.T., R.K.); Mitsubishi Pharma Research Foundation (S.O., M.S.); and Research for Promoting Technological Seeds A (discovery type) (S.O.); Yokohama Academic Foundation (S.O.); 2010 Commercialization Promotion Program for Biotechnology-related Studies (S.O.); Grant for Research and Development Project II (No. 8 and 14) of Yokohama City University (Y.I., S.O.); and Research Foundation for Community Medicine (S.O.).

References

1 Murray KJ, Reeves ML, England PJ. Protein phosphorylation and compartments of cyclic AMP in the control of cardiac contraction. Mol Cell Biochem. 1989;89:175–179.
2 Federman AD, Conklin BR, Schrader KA, Reed RR, Bourne HR. Hormonal stimulation of adenylyl cyclase through Gi-protein $\beta\gamma$ subunits. Nature. 1992;356:159–161.
3 Ishikawa Y, Homcy CJ. The adenylyl cyclases as integrators of transmembrane signal transduction. Circ Res. 1997;80:297–304.
4 Ishikawa Y. Regulation of cAMP signaling by phosphorylation. Adv Second Messenger Phosphoprotein Res. 1998;32:99–120.
5 Hanoune J, Defer N. Regulation and role of adenylyl cyclase isoforms. Annu Rev Pharmacol Toxicol. 2001;41:145–174.
6 Caulfield MP, Robbins J, Higashida H, Brown DA. Postsynaptic actions of acetylcholine: the coupling of muscarinic receptor subtypes to neuronal ion channels. Prog Brain Res. 1993;98: 293–301.
7 Okumura S, Kawabe J, Yatani A, Takagi G, Lee MC, Hong C, et al. Type 5 adenylyl cyclase disruption alters not only sympathetic but also parasympathetic and calcium-mediated cardiac regulation. Circ Res. 2003;93:364–371.
8 Okumura S, Takagi G, Kawabe J, Yang G, Lee MC, Hong C, et al. Disruption of type 5 adenylyl cyclase gene preserves cardiac function against pressure overload. Proc Natl Acad Sci

U S A. 2003;100:9986–9990.
9 Okumura S, Vatner DE, Kurotani R, Bai Y, Gao S, Yuan Z, et al. Disruption of type 5 adenylyl cyclase enhances desensitization of cyclic adenosine monophosphate signal and increases Akt signal with chronic catecholamine stress. Circulation. 2007;116:1776–1783.
10 Di Rienzo M, Castiglioni P, Iellamo F, Volterrani M, Pagani M, Mancia G, et al. Dynamic adaptation of cardiac baroreflex sensitivity to prolonged exposure to microgravity: data from a 16-day spaceflight. J Appl Physiol. 2008;105:1569–1575.
11 Abe C, Tanaka K, Awazu C, Morita H. Impairment of vestibular-mediated cardiovascular response and motor coordination in rats born and reared under hypergravity. Am J Physiol Regul Integr Comp Physiol. 2008;295:R173–R180.
12 Iwasaki K, Shiozawa T, Kamiya A, Michikami D, Hirayama K, Yajima K, et al. Hypergravity exercise against bed rest induced changes in cardiac autonomic control. Eur J Appl Physiol. 2005;94:285–291.
13 Okumura S, Tsunematsu T, Bai Y, Qian J, Ono S, Suzuki S, et al. Type 5 adenylyl cyclase plays a major role in stabilizing heart rate in response to microgravity induced by parabolic flight. J Appl Physiol. 2008;105:173–179.
14 Toya Y, Schwencke C, Ishikawa Y. Forskolin derivatives with increased selectivity for cardiac adenylyl cyclase. J Mol Cell Cardiol. 1998;30:97–108.
15 Iwatsubo K, Minamisawa S, Tsunematsu T, Nakagome M, Toya Y, Tomlinson JE, et al. Direct inhibition of type 5 adenylyl cyclase prevents myocardial apoptosis without functional deterioration. J Biol Chem. 2004;279:40938–40945.
16 Malik M, Bigger JT, Camm AJ, Kleiger RE, Malliani A, Moss AJ, et al; Task force of the European society of cardiology and the north American society of pacing and electrophysiology. Heart rate variability. Standards of measurement, physiological interpretation, and clinical use. Eur Heart J. 1996;17:354–381.
17 Young LR, Oman CM, Watt DG, Money KE, Lichtenberg BK. Spatial orientation in weightlessness and readaptation to earth's gravity. Science. 1984;225:205–208.
18 Buckey JC Jr, Lane LD, Levine BD, Waterpaugh DE, Wright SJ, Moore WE, et al. Orthostatic intolerance after spaceflight. J Appl Physiol. 1996;81:7–18.
19 Fritsch-Yelle JM, Whitson PA, Bondar RL, Brown TE. Subnormal norepinephrine release relates to presyncope in astronauts after spaceflight. J Appl Physiol. 1996;81:2134–2141.
20 Seps B, Beckers F, Aubert AE. Heart rate variability during gravity transitions. Comput Cardiol. 2002;29:433–436.
21 Gehrmann J, Berul CI. Cardiac electrophysiology in genetically engineered mice. J Cardiovasc Electrophysiol. 2000;11:354–368.
22 Tepe NM, Liggett SB. Transgenic replacement of type V adenylyl cyclase identifies a critical mechanism of β-adrenergic receptor dysfunction in the Gαq overexpressing mouse. FEBS Lett. 1999;458:236–240.
23 Levine BD, Pawelczyk JA, Ertl AC, Coz JF, Zuckermann JH, Diedrich A, et al. Human muscle sympathetic neural and haemodynamic responses to tilt following spaceflight. J Physiol. 2002;538:331–340.
24 Kamen PW, Krum H, Tonkin AM. Poincare plot of heart rate variability allows quantitative display of parasympathetic nervous activity in humans. Clin Sci (Lond). 1996;91:201–208.
25 Migeotte PF, Prisk GK, Paiva M. Microgravity alters respiratory sinus arrhythmia and short-term heart rate variability in humans. Am J Physiol Heart Circ Physiol. 2003;284:H1995–H2006.
26 Verheyden B, Beckers F, Aubert AE. Spectral characteristics of heart rate fluctuations during parabolic flight. Eur J Appl Physiol. 2005;95:557–568.
27 Tobise K, Ishikawa Y, Holmer SR, Im MJ, Newell JB, Yoshine H, et al. Changes in type VI adenylyl cyclase isoform expression correlate with a decreased capacity for cAMP generation in the aging ventricle. Circ Res. 1994;74:596–603.
28 Espinasse I, Iourgenko V, Defer N, Salmon F, Hanoune J, Mercadier JJ. Type V, but not type VI, adenylyl cyclase mRNA accumulates in the rat heart during ontogenic development. Correlation with increased global adenylyl cyclase activity. J Mol Cell Cardiol. 1995;27:1789–1795.
29 Tang T, Lai NC, Roth DM, Drumm J, Guo T, Lee KW, et al. Adenylyl cyclase type V deletion increases basal left ventricular function and reduces left ventricular contractile responsiveness to β-adrenergic stimulation. Basic Res Cardiol. 2006;101:117–126.
30 Gao MH, Lai NC, Roth DM, Zhou J, Zhu J, Anza T, et al. Adenylylcyclase increases responsiveness to catecholamine stimulation in transgenic mice. Circulation. 1999;99:1618–1622.
31 Tepe NM, Lorenz JN, Yatani A, Dash R, Kranias EG, Dorn GW II, et al. Altering the receptor-effector ratio by transgenic overexpression of type V adenylyl cyclase: enhanced basal catalytic activity and function without increased cardiomyocyte β-adrenergic signalling. Biochemistry. 1999;38:16706–16713.

NeuroImage 70 (2013) 10–20

Contents lists available at SciVerse ScienceDirect

NeuroImage

journal homepage: www.elsevier.com/locate/ynimg

Systematic changes to the apparent diffusion tensor of in vivo rat brain measured with an oscillating-gradient spin-echo sequence

Jeff Kershaw [a,b,*], Christoph Leuze [c], Ichio Aoki [a], Takayuki Obata [d], Iwao Kanno [a], Hiroshi Ito [a], Yuki Yamaguchi [b], Hiroshi Handa [b]

[a] Molecular Imaging Center, National Institute of Radiological Sciences, Chiba, Japan
[b] School of Bioscience and Biotechnology, Tokyo Institute of Technology, Yokohama, Japan
[c] Department of Neurophysics, Max Planck Institute for Human Cognitive and Brain Sciences, Leipzig, Germany
[d] Research Centre for Charged Particle Therapy, National Institute of Radiological Sciences, Chiba, Japan

ARTICLE INFO

Article history:
Accepted 12 December 2012
Available online 27 December 2012

Keywords:
Oscillating-gradient spin-echo
Apparent diffusion tensor
In vivo rat brain
Tissue microstructure
Effective diffusion-time
Restricted diffusion

ABSTRACT

As the oscillating gradient spin-echo sequence has shown promise as a means to probe tissue microstructure, it was applied here to diffusion-tensor imaging of in vivo rat brain. The apparent diffusion tensor (ADT) was estimated for motion-probing gradient (MPG) frequencies in the range 33.3–133.3 Hz, and regions-of-interest (ROIs) in the corpus callosum (CC), visual cortex (VC), cerebellar white matter (CBWM) and cerebellar grey matter (CBGM) were selected for detailed analysis. There were substantial, approximately linear changes to the ADT with increasing MPG frequency for all four ROIs. All ROIs showed clear increases in mean diffusivity. CBWM had a substantial decrease in fractional anisotropy, whereas the CC and VC had minor increases of the same parameter. All eigenvalues of the ADT tended to increase with frequency for the CBWM, CBGM and VC, but only the principal eigenvalue increased strongly for the CC. On the other hand, there was no evidence that the orientation of the principal eigenvector varied systematically with MPG frequency for any of the ROIs. The relationship between the behaviour of the eigenvalues and the behaviours of the mean diffusivity and fractional anisotropy is investigated in detail. Pixelwise linear fits to the MD from individual animals found elevated changes across the cerebellum. The data acquired for this work encompassed a range of effective diffusion-times from 7.5 ms down to 1.875 ms, and some ideas on how the results might be used to extract quantitative information about brain tissue microstructure are discussed.

Introduction

Many studies with diffusion-weighted MRI have indicated that manipulating the parameters of the motion-probing gradients (MPGs) offers a noninvasive means to probe in vivo tissue microstructure. One parameter routinely modified to alter image contrast is the orientation of the MPGs. Cycling the MPG direction around a hemisphere while preserving other parameters is used in diffusion-tensor MRI (DTI) (Basser et al., 1994) and other techniques like q-ball (Tuch, 2004) and HARDI (Tuch et al., 2002) to investigate tissue anisotropy. Another parameter with the potential to modify image contrast is the diffusion-time. Modulating the diffusion-time is often cited as a means to investigate restricted or hindered diffusion in complex media, but it is widely neglected in clinical situations because evidence for distinct, unequivocal contrast changes in vivo is sparse.

Most studies investigating the effects of varying diffusion-time on image contrast in diffusion-weighted MRI have been performed with conventional pulsed-gradient spin-echo (PGSE) and pulsed-gradient stimulated-echo (PGStE) sequences. Using these sequences, changes to the signal with decreasing diffusion-time have been found in a variety of biological systems, including in vitro cell cultures (Pilatus et al., 1997), ex vivo rat brain (Assaf and Cohen, 1998) and in vivo radiation-induced tumors (Helmer et al., 1995). In vivo experiments on normal tissue have also been performed, but, with two exceptions, the studies were limited to diffusion-times of 8 ms or longer and no significant signal changes were observed (Clark et al., 2001; Le Bihan et al., 1993; Moonen et al., 1991; Niendorf et al., 1996; van Gelderen et al., 1994). One of the exceptions reported changes for diffusion-times in the range 33.3–793.3 ms (Horsfield et al., 1996). However, as the *b*-value of a sequence is not independent of the diffusion-time and no precautions seem to have been taken to keep the *b*-value constant, other researchers have questioned whether

Abbreviations: OGSE, oscillating gradient spin-echo; DTI, diffusion-tensor imaging; PGSE, pulsed-gradient spin-echo; PGStE, pulsed-gradient stimulated-echo; MPG, motion-probing gradient; ADT, apparent diffusion tensor; ADC, apparent diffusion coefficient; MD, mean diffusivity; FA, fractional anisotropy; EV, eigenvalue; ROI, region of interest; CBWM, cerebellar white matter; CBGM, cerebellar grey matter; CC, corpus callosum; VC, visual cortex; CBGr, cerebellar granular layer.

* Corresponding author at: Molecular Imaging Center, National Institute of Radiological Sciences, 4-9-1 Anagawa, Inage-ku, Chiba 263-8555 Japan. Fax: +81 43 206 0819.
E-mail address: len@nirs.go.jp (J. Kershaw).

1053-8119/$ – see front matter © 2012 Elsevier Inc. All rights reserved.
http://dx.doi.org/10.1016/j.neuroimage.2012.12.036

the observed signal changes can be unambiguously attributed to a diffusion-time dependent effect (Clark et al., 2001; Does et al., 2003). In the second exception, a bipolar MPG was placed in only the first half of the echo-time so that diffusion-times as low as 1.6 ms were possible (Niendorf et al., 1994). At a constant b-value of 210 s/mm^2, the signal was found to decrease as the diffusion-time was reduced from 5.9 to 3.4 ms, suggesting that diffusion-time related contrast changes can be observed in vivo if the diffusion-time is less than around 5 ms, something that is difficult to achieve with standard PGSE and PGStE sequences.

As an alternative to PGSE and PGStE, the oscillating-gradient spin-echo (OGSE) sequence has been proposed as a means to reach diffusion-times of less than 5 ms (Gross and Kosfeld, 1969; Schachter et al., 2000). While OGSE was originally implemented with sinusoidal MPGs, more recent versions employ an apodised cosinusoidal shape (Does et al., 2003; Parsons et al., 2003). For an apodised cosinusoidal MPG of dominant frequency f, an effective diffusion-time of $1/4f$ can be improvised by equating the b-values calculated for the PGSE and OGSE sequences. Under this prescription, OGSE has been used to observe diffusion-time dependent signal changes and subsequently estimate the surface-to-volume ratio in systems of packed beads (Parsons et al., 2003; Parsons et al., 2006). It has also been employed to investigate intracellular restriction effects in in vitro cell preparations (Colvin et al., 2011; Xu et al., 2011), and, most importantly, demonstrate diffusion-time dependent signal changes in normal and diseased rat brain in vivo (Colvin et al., 2008; Does et al., 2003). Even though it has recently been pointed out that the effective diffusion-time construct only applies over a limited range of frequencies (Novikov and Kiselev, 2011), it has nonetheless been firmly established that OGSE provides a unique image contrast and is therefore a promising technique for probing in vivo tissue microstructure.

In most previous studies with the OGSE sequence, little consideration has been given to the consequences of varying MPG orientation. If frequency-dependent effects are observable when the MPG is applied in one direction, it follows that combining orientation and frequency modulated experiments may provide an interesting new method to investigate tissue properties. A similar idea has already been considered for the PGSE and PGStE sequences, but in terms of the diffusion-time. For example, the diffusion-time dependence of the mean diffusivity (MD), which is the trace of the apparent diffusion tensor (ADT) divided by 3, has been investigated with those sequences in several studies (e.g. Le Bihan et al., 1993; Horsfield et al., 1996). In those cases, however, data was only acquired in the three principal gradient directions so that the full ADT and apparent anisotropy could not be estimated. The only study where the dependence of the full ADT on diffusion-time has been investigated was that by Clark et al. (2001), who found no changes to the ADT, possibly because the shortest diffusion-time employed in the study (8 ms) was too long. With the introduction of the OGSE sequence, it seems possible that alterations to the ADT with diffusion-time may be observable if the correspondence between MPG frequency and effective diffusion-time is utilised. The only earlier applications of this idea were to ex vivo monkey brain (Xu et al., 2010) and ex vivo mouse brain (Aggarwal et al., 2012). The goal of this study was to combine OGSE with DTI-like acquisition and analysis protocols to investigate the MPG frequency dependence of the ADT in rat brain in vivo. An interpretation of the results in terms of restricted diffusion and the effective diffusion-time is also considered. Some of the results have been previously presented in abstract form (Kershaw et al., 2010, 2011).

Materials and methods

All experiments were approved by the Animal Welfare Committee of the National Institute of Radiological Sciences, Chiba, Japan.

Eleven male Sprague–Dawley rats (age 7–9 weeks, weight 200–300 g) were anaesthetised with isoflurane (4% for induction and 2% during the imaging experiments) and fixed in a MRI compatible cradle with bite and ear bars. The cradle was inserted into the bore of the magnet and then rotated so that the animal was upside-down to minimise the effects of respiratory motion. Rectal temperature was maintained at around 37 °C with heated air throughout the experiment. All MRI data were acquired on a 7 T MRI system (Magnet: Kobelco, Japan; Console: Bruker Avance I, Germany) equipped with an actively-screened gradient system (Bruker BGA12). A volume coil (diameter 72 mm, Bruker) was used for transmission and a 2-channel phased-array surface coil (13 mm × 15 mm, Rapid Biomedical, Germany) was used for signal reception. The latter coil was positioned over the head of the animal centred near the interaural plane to maximise the signal received from both the cerebellum and caudal end of the cerebrum.

Data acquisition was performed with a four-shot SE-EPI sequence modified to have one apodised cosinusoidal MPG waveform placed on either side of the π-refocussing pulse (Does et al., 2003; Parsons et al., 2003; Colvin et al., 2008). The sequence was set up so that the user first selects the duration T of the MPG lobes, which determines the base frequency $f = 1/T$, and then the desired harmonics of f and the maximum b-value are entered. The b-value as a function of frequency is $(\gamma G_k/2\pi f_k)^2(1-1/8k)T$, where $f_k = kf$ is the frequency of the kth harmonic and G_k is the peak amplitude of the applied MPG (Does et al., 2003; Parsons et al., 2003). The code automatically set G_k so that b remains constant with increasing k. The code was also configured so that $b = 0$ data was acquired when a value of zero was included in the list of harmonics. After choosing the harmonics, the user selected the number of directions in which to apply the oscillating MPGs. Unit vectors defining the directions were either entered by hand or read in from a set of prepared files. Acquisition of the data for a single experiment then proceeded in two major loops: the outer loop cycled through the MPG directions and the inner loop cycled through the list of selected harmonics.

A 1 mm thick sagittal slice set at 1–1.5 mm away from the midplane of the brain was selected for imaging. This orientation and position ensured that the slice passed through both the cerebellum and the thickest part of the corpus callosum. Three experiments, distinguished by different sets of MPG parameters, were performed on each animal (see Table 1). Note that the selected harmonics were limited to those where G_k did not exceed 91% of the maximum available gradient (404 mT/m). Each experiment acquired images for 78 evenly distributed MPG directions. Other common imaging parameters were TR = 3 s, matrix size = 128 × 128, FOV = 25.6 mm × 25.6 mm, and spatial resolution = 0.2 mm × 0.2 mm × 1 mm. T_2-weighted anatomical images of the same slice were also acquired with a standard multi-SE sequence (TR = 3 s, 14 echoes, TE = 10–140 ms).

The data was reconstructed and analysed offline using purpose-written Matlab code. No spatial or temporal smoothing was applied at any point during the analysis. The six independent elements of the ADT were estimated pixel-by-pixel for each harmonic from each experiment on each animal using a standard DTI analysis technique (Basser et al., 1994). Partially guided by the MD and fractional anisotropy (FA) maps calculated from the lowest frequency data of the type A experiments listed in Table 1, regions-of-interest (ROIs) were drawn by hand on the anatomical images of each animal. The same ROIs

Table 1
Oscillating MPG parameters for the three experiments performed on each animal.

Expt	TE (ms)	T (ms)	Max b (s/mm^2)	k	f_k (Hz)
A	71	26	1000	1, 2	38.5, 76.9
B	71	26	450	1, 2, 3	38.5, 76.9, 115.4
C	79	30	400	1, 2, 3, 4	33.3, 66.6, 100, 133.3

were used for all experiments on a particular animal. After averaging across the ROIs and collecting the data from all animals, the frequency dependence of the MD, FA and eigenvalues (EVs) of the ADT were evaluated. In addition, possible alteration to the orientation of the ADT with MPG frequency was investigated by grouping the principal eigenvectors of the ADT from all experiments by frequency, and then applying a parametric analysis-of-variance-like hypothesis test devised for groups of unit vectors on a sphere (Schwartzman et al., 2005; Mardia and Jupp, 2000).

All parameter estimation was performed with conventional multivariate linear least-squares fitting. Uncertainty in the parameter estimates was determined by bootstrapping the original data set (Efron and Tibshirani, 1994). Apart from the dependence on MPG frequency, it is possible that animal differences and the effects of other imaging parameters, such as the maximum b-value or TE, might also affect the ADT. Even so, multiple harmonics were acquired during each experiment and analysis of the data found that the trend with frequency was similar across experiments and animals. For that reason, the uncertainty of the estimates was evaluated by randomly sampling from the pool of experiments rather than the full data set as independent points. In practice, this means that when a data point from a particular experiment was randomly sampled, all data from that experiment was also included. In this way the variation contributed by differences between animals or imaging parameters is accounted for and the true uncertainty associated with the frequency dependence can come to the fore.

Results

Water and asparagus samples

To verify that the OGSE DTI protocol produces sensible results in a model system, it was first applied to pure water and asparagus samples (Fig. 1). Consistent with expectations, the MD (Fig. 1a), FA (Fig. 1b) and EVs (Fig. 1c) of the ADT estimated from the water data are insensitive to MPG frequency in the range 15–170 Hz. Regardless of frequency the MD had a value of around $2\mu m^2$/ms, which is close to the value expected for the diffusion coefficient of water at room temperature. Similarly, the FA was estimated to be approximately 0.04 for all frequencies. The near isotropy of the water sample is reinforced by the similarity of the three EVs across frequencies.

In contrast, the results from the asparagus data show that the ADT is dependent on MPG frequency in the presence of microstructure. The MD of the asparagus increases with MPG frequency towards the water value (Fig. 1a). At the same time, the FA decreases from $\approx$0.26 at 25 Hz to $\approx$0.1 at 150 Hz (Fig. 1b). The EVs are plotted in Fig. 1d. At the lowest MPG frequency, the relatively large difference between the largest EV (blue) and each of the two smaller EVs (green and red) is consistent with the expected anisotropy of water motion in asparagus. However, while the largest EV remains approximately constant, the smaller EVs increase with MPG frequency and thus the apparent anisotropy decreases accordingly.

In vivo rat studies

Figs. 2a and b are the MD and FA maps, respectively, from a typical rat. The results are similar to what might be observed with standard PGSE or PGStE sequences. Arrows on the FA image point to the higher FA of the cerebellar white matter (CBWM) and the splenium of the corpus callosum (CC). Taking these two areas as ROIs with high apparent anisotropy, and adding cerebellar grey matter (CBGM) and visual cortex (VC) ROIs as examples of tissue with lower anisotropy (Fig. 2c), it is desired to analyse the frequency dependence of the ADT in those areas. Note that the $b=0$ images typically had signal-to-noise ratios of ~15–20 in the visual cortex and ~10–15 for the cerebellar ROIs.

The mean and standard deviation of the MD across experiments are plotted against MPG frequency in Fig. 3. Even though the MDs calculated for different experiments and animals may have varied by around 10–30%, the MD from any experiment tended to show the same trend with frequency for all ROIs. From inspection it appears that there is an upward trend of the MD with frequency for the

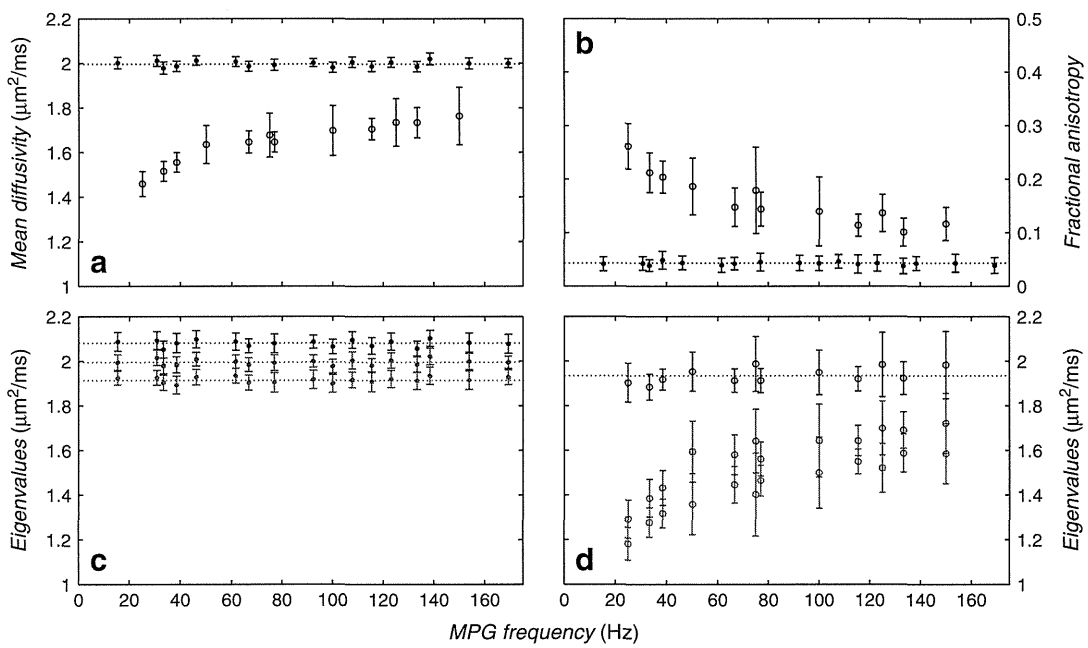

Fig. 1. The OGSE DTI protocol applied to pure water (closed circles) and asparagus (open circles) samples. (a) Mean diffusivity. (b) Fractional anisotropy. (c) Eigenvalues for the water data. (d) Eigenvalues for the asparagus data. The water data is insensitive to MPG frequency while the signal from the asparagus demonstrates a clear dependence on frequency. The error bars correspond to the standard deviation across the selected ROIs.

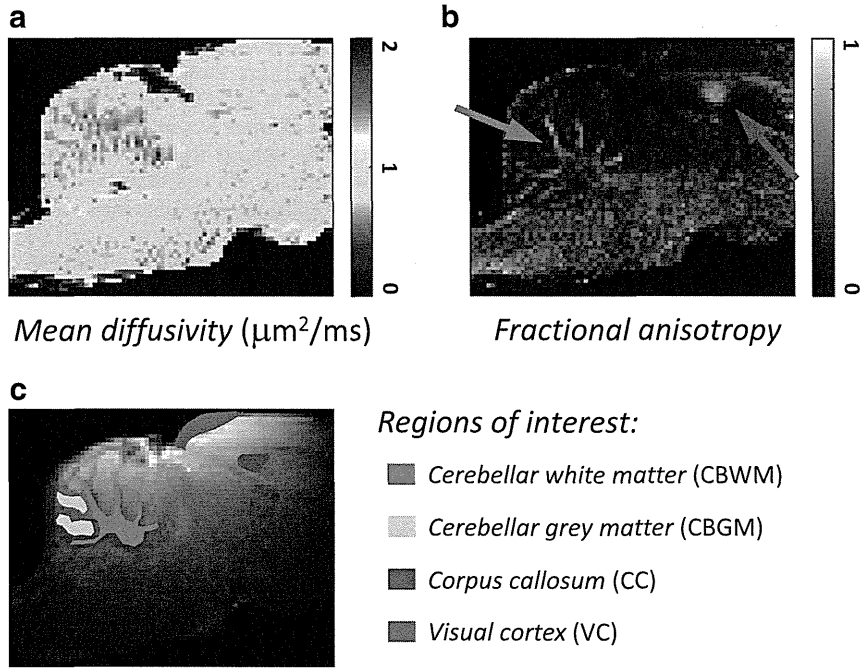

Fig. 2. OGSE DTI (a) MD and (b) FA maps from a typical rat. Note the arrows pointing to the higher FAs of the cerebellar white matter (CBWM) and splenium of the corpus callosum (CC) in (b). (c) The frequency dependence of the ADT was analysed in detail for regions-of-interest in the CBWM, cerebellar grey matter (CBGM), CC and visual cortex (VC).

CBWM and CBGM, and perhaps for the other ROIs as well. As the increase appears to be approximately linear over the range of frequencies used, the change in MD was characterised by fitting a straight line $\alpha_{MD}f+\beta_{MD}$ to the data with linear least-squares. If there is a significant change to the MD with frequency then the slope α_{MD} of the fitted line should be significantly different from zero. The fitted lines are plotted on top of the data in Fig. 3 and the estimates for α_{MD} are presented in Fig. 4a. The estimates for all four ROIs are positive. Moreover, the 95% confidence intervals obtained from bootstrapping the data do not overlap zero. Therefore, it is possible to conclude that the MD increases significantly for each ROI, although more so for the CBWM and CBGM ROIs than for the CC and VC ROIs.

Fig. 5 similarly presents the mean and standard deviation of the FA across experiments plotted against MPG frequency. The behaviour of this data with MPG frequency was also characterised by a fit to a straight line. The fitted lines are plotted on top of the data in Fig. 5

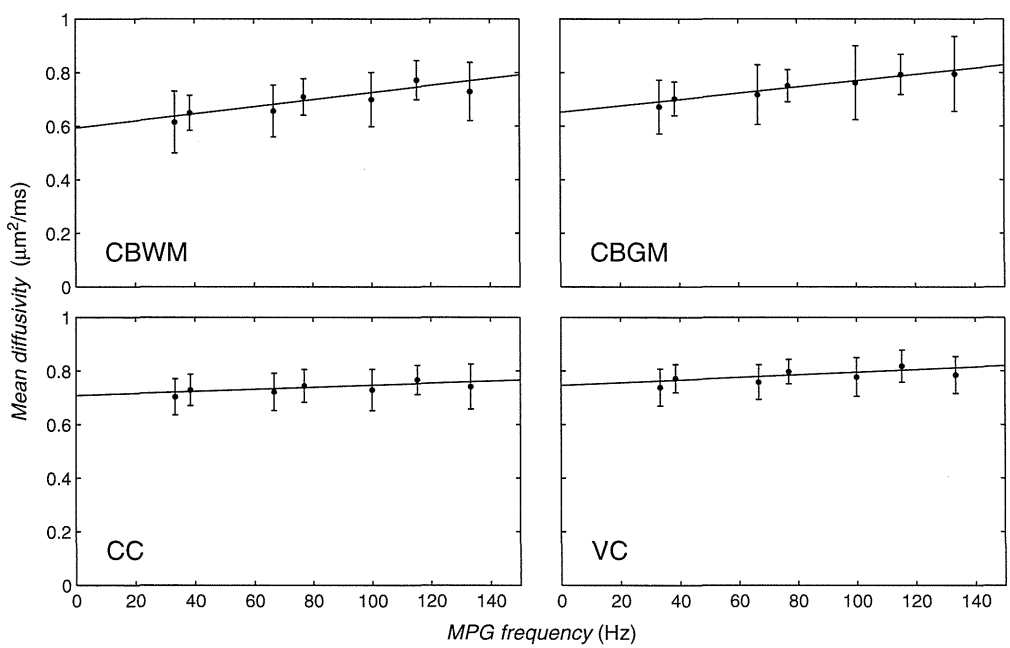

Fig. 3. MD plotted against MPG frequency for all four ROIs. The error bars represent the standard deviation of the MD across animals and experiments at the same frequency. The CBWM and CBGM appear to have a clear upward trend with increasing frequency. The solid lines are straight line fits to the data, with the estimates and uncertainty of the slopes shown in Fig. 4a.

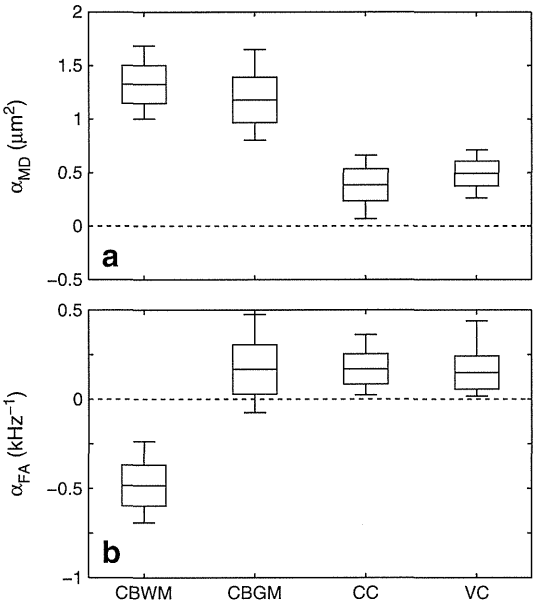

Fig. 4. Box-whisker plots of (a) α_{MD} and (b) α_{FA} estimated from straight-line fits with respect to MPG frequency for all ROIs. The boxes represent the standard deviation of the estimates and the thinner bars are the 95% confidence intervals.

and the estimates for the slope, α_{FA}, are presented in Fig. 4b. The estimate for the CBWM ROI is significantly less than zero, indicating a substantial decrease of FA with frequency in this ROI. While the 95% confidence interval of the CBGM indicates that the FA was independent of frequency for that ROI, the intervals for the CC and VC narrowly exclude zero, suggesting a minor increase of the apparent anisotropy in those ROIs.

The EVs of the ADT are presented in Fig. 6. Note that there is a more pronounced separation between the largest and two smaller EVs of the CBWM and CC than there is for the CBGM and VC. This difference is the source of the higher apparent anisotropies of the CBWM and CC. Changes to the EVs with MPG frequency were again characterised with a straight line fit and the estimates for the slope (α_{λ_i}, $i=1,2,3$) are shown in Fig. 7. The estimates of the α_{λ_i} for the CBWM and CBGM ROIs are significantly greater than zero, which means that all three EVs in those areas are increasing with MPG frequency. The same is true for the EVs of the VC ROI, although the rates of increase are less than those for the CBWM and CBGM and the 95% confidence interval of the smallest EV only narrowly excludes zero. For the CC ROI, while the largest EV increases significantly with frequency, both the second and third EVs are relatively unaffected in comparison.

Fig. 8 provides a simple graphical illustration of the dependence of the principal eigenvectors on frequency for all ROIs. Note that the CC has a very tight formation that makes it difficult to distinguish individual points, while the spread of the CBWM and CBGM eigenvectors is less dense but still well localised. The compact nature of these distributions suggests that they might be described by bipolar Watson distributions (Mardia and Jupp, 2000). In contrast, the VC eigenvectors are better described by a girdle-like Watson distribution because the data is spread along a circumference of the sphere. Grouping the eigenvectors by frequency and taking the null hypothesis to be the assumption that the mean directions of the groups are equal, the consistency in orientation of the principal eigenvectors was evaluated by applying a hypothesis test based on a Watson distribution of the appropriate type for each ROI. As presented in Table 2, all ROIs have *P*-values greater that 0.5 so there is no strong basis to reject the null hypothesis. In support of this, the black solid lines on Fig. 8 indicate that the mean directions of the ROIs did not evolve with frequency in any obvious systematic way.

Discussion

There were substantial, approximately linear changes to the rat ADT with increasing MPG frequency for all four in vivo ROIs. The ADT in the CBWM demonstrated strong increases to the EVs and MD, as well as a significant decrease in the FA. Both the CBGM and VC had significant increases in the EVs and MD, but there was no or only a minor change to the FA. The situation was more complex for

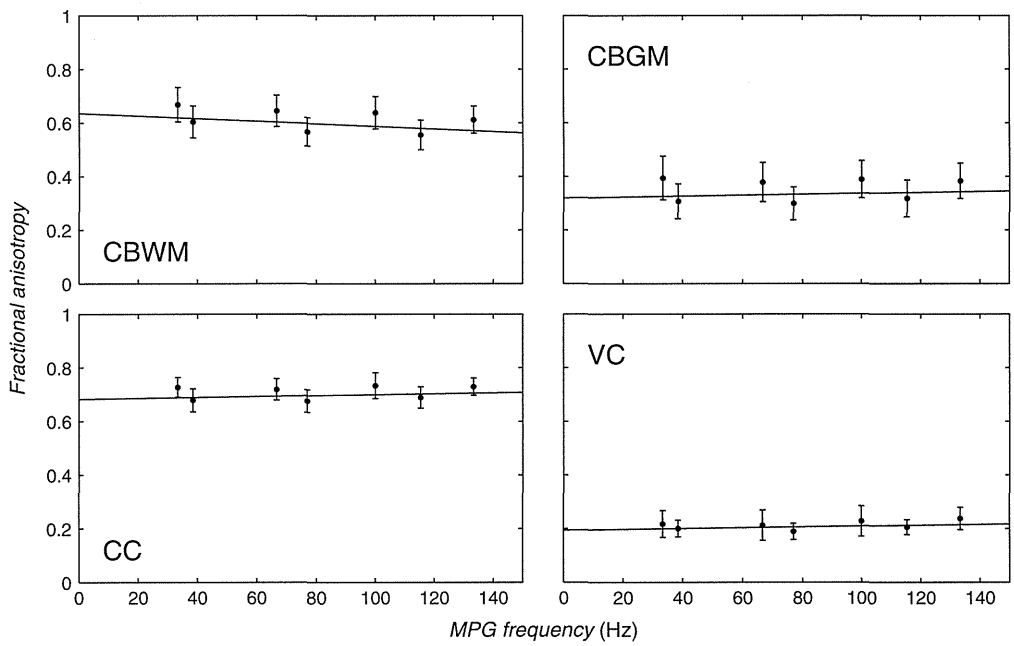

Fig. 5. FA plotted against MPG frequency for all four ROIs. The error bars represent the standard deviation of the FA across animals and experiments at the same frequency. The CBWM has a clear downward trend with increasing frequency. The solid lines are straight line fits to the data, with the estimates and uncertainty of the slopes shown in Fig. 4b.

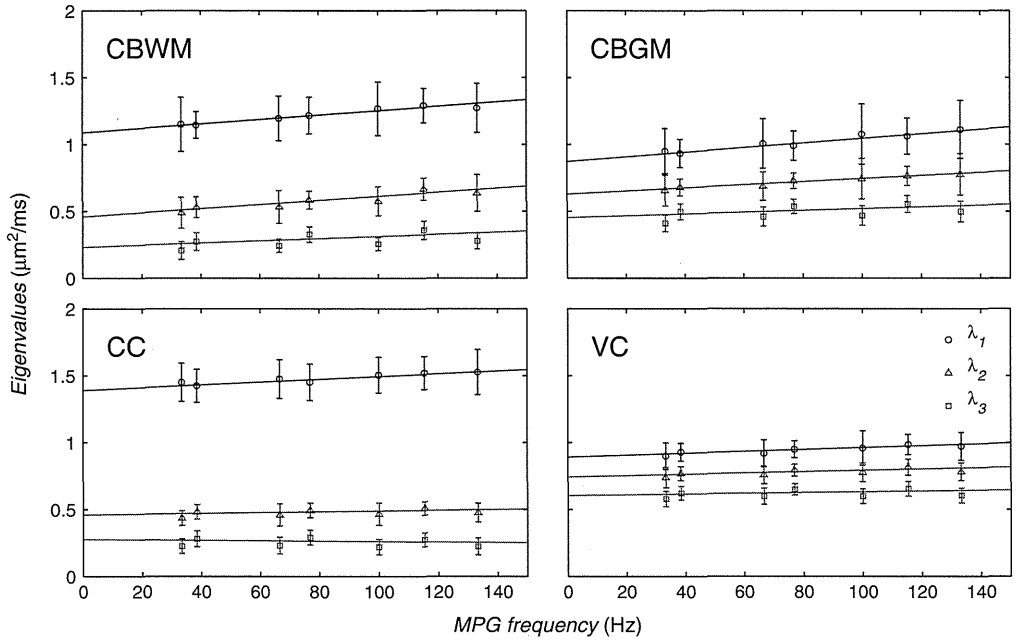

Fig. 6. The EVs of the ADT plotted against MPG frequency for all four ROIs. The error bars represent the standard deviation of the EVs across animals and experiments at the same frequency. The solid lines are straight line fits to the data, with the estimates and uncertainty of the slopes shown in Fig. 7.

the CC as minor increases to the MD and FA corresponded to a strong increase in the first EV, but only minor or no changes to the two smaller EVs. At the same time, there was no clear indication that the orientation of the principal eigenvectors varied systematically with the applied frequency for any of the ROIs.

Comparison with previous OGSE DTI of brain tissue

Recent OGSE DTI observations made by Aggarwal et al. (2012) on ex vivo mouse brains over the range 50–150 Hz also found that the MD (denoted by ADC in that study), FA and EVs varied linearly with MPG frequency. They also found no evidence that the primary direction of the ADT was altered with frequency. The most dramatic dependences on frequency were observed in the granule cell layer of the dentate gyrus, the pyramidal cell layer of the hippocampus, and the cerebellar granule cell layer (CBGr). By performing pixelwise linear fits with respect to MPG frequency, it was demonstrated that maps of the slope provide a novel tissue contrast in diffusion-weighted MRI of mouse brain. While it was not clear what the mechanism driving the contrast change is, comparison to immunohistochemical staining found that regions with enhanced MD largely correspond to areas with densely-packed neurons having relatively large nuclei. From this result and simulations performed with a simplified model of cell structure (Xu et al., 2009), it was suggested

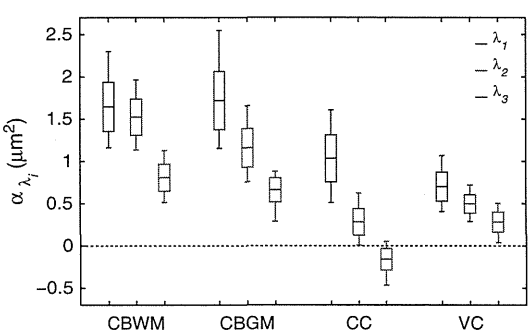

Fig. 7. Box-whisker plots of the α_{λ_i} estimated from straight-line fits to the EVs of the ADT with MPG frequency for all ROIs. The boxes represent the standard deviation of the estimates and the thinner bars are the 95% confidence intervals.

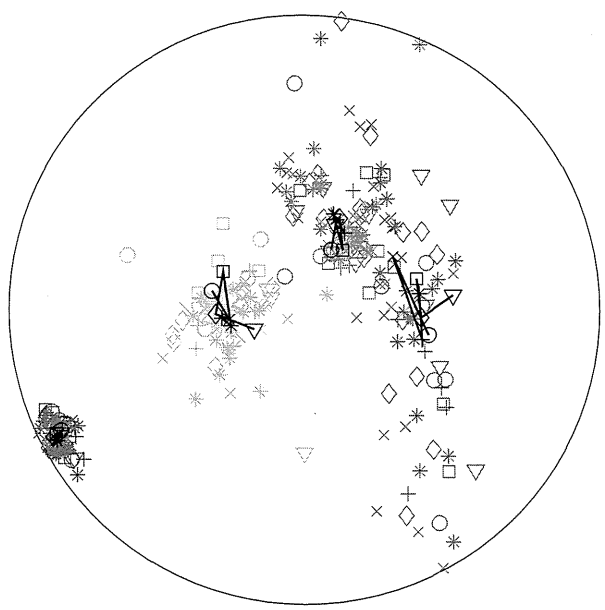

Fig. 8. Lambert equal-area projection of the principal eigenvectors of all ROIs onto the tangent plane passing through the point (0.48, 0.48, 0.73) on a unit sphere. Each point represents where the tip of a particular eigenvector lies on the sphere. The region inside the black circle is an area-preserving map of the upper hemisphere onto the plane. Points have been plotted using the same colour scheme originally used in Fig. 2. The eigenvectors from each ROI have been grouped according to MPG frequency with the following correspondences between the symbols and frequency: ○, 33.33 Hz; ×, 38.5 Hz; +, 66.6 Hz; ✳, 76.9 Hz; □, 100 Hz; ◇, 115.4 Hz; ▽, 133.3 Hz. The black symbols and lines illustrate the progression of the mean direction with frequency for each ROI. The points are joined in the order of increasing frequency, but there does not appear to be any simple deterministic pattern to the arrangements. The results of a hypothesis test evaluating the consistency of the mean directions with frequency are presented in Table 2.

Table 2
P-values from hypothesis tests evaluating the consistency of the principal eigenvector orientation with MPG frequency. The hypothesis tests for the CBWM, CBGM and CC were based on a bipolar Watson distribution, and that for the VC was based on a girdle-like Watson distribution (Mardia and Jupp, 2000).

ROI	CBWM	CBGM	CC	VC
P	0.31	0.056	0.19	0.057

that α_{MD} may be correlated with the nuclear volume fractions of the cells in those regions.

As there is a clear correspondence between the morphology of the rat and mouse brains, a similar pixelwise linear fit to the data from individual animals was performed to investigate whether changes to the MD can be discerned across the area imaged in the present research. The example presented in Fig. 9 shows no obvious changes in the visual cortex, corpus callosum or other parts of the caudal cerebrum, but there is a clear elevation of α_{MD} across the cerebellum. Enhanced pixels have α_{MD}s in the range 2–4 μm^2, which is ~2–3 times larger than the values found for the CBWM and CBGM ROIs (but similar to the value of 3.6 μm^2 estimated from Fig. 4c of Aggarwal et al. (2012) for the CBGr in ex vivo mouse cerebellum; see Supplementary Table 1). Unfortunately, the contrast is not sharp enough and the resolution too coarse to unequivocally attribute the enhancement to a specific tissue type by eye. Moreover, the histograms in Fig. 9b demonstrate that there was no exclusive correspondence between pixels with elevated α_{MD} and one or other of the cerebellar ROIs. If the source of this in vivo enhancement is the same as the ex vivo CBGr enhancement found by Aggarwal et al. (2012), then the granular cells may have influenced both the CBWM and CBGM results. Fig. 10 presents sagittal histological sections from an 8 week old rat. As well as the CBGr, the grey region in the cerebellum consists of two other cellular layers with distinct structural characteristics: a single layer of Purkinje cells and a superficial molecular layer. The Purkinje

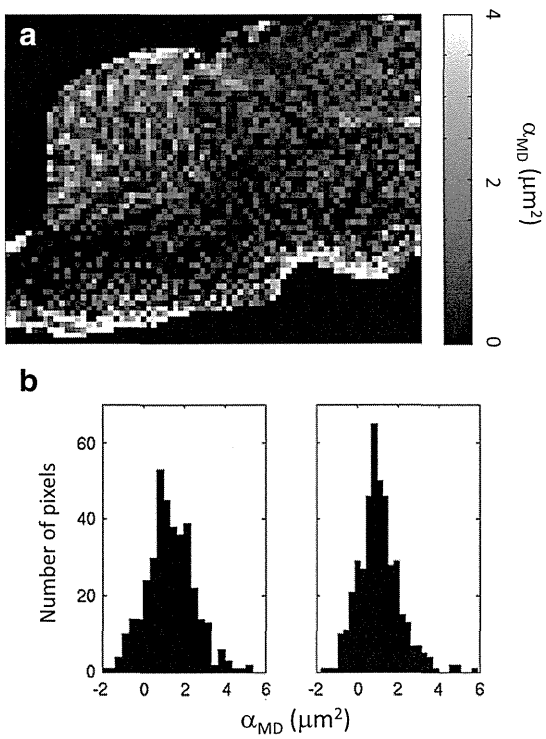

Fig. 9. (a) Map of α_{MD} for the same rat as shown in Fig. 2. Note the enhanced values in the cerebellum. (b) The α_{MD}s of all pixels in the CBWM and CBGM ROIs of all animals have been placed in histograms to demonstrate that pixels with elevated values were not exclusive to either ROI.

layer is probably too thin to have a significant effect on the diffusion-weighted signal so that the granular and molecular layers most likely dominate any signal changes. Pixels selected for the CBGM ROI were located in the prepyramidal and secondary fissures of the cerebellum at least one pixel away from any pixels considered to be white matter, but there was no way to differentiate between the CBGr and molecular layers. At the same time, the criteria for CBWM pixels was that they had FAs of 0.5–0.8 and were clearly located in the regions commonly designated as white matter on T_2-weighted images. However, in the sagittal orientation the white matter branches in the lobules of adult rat cerebellum are at most 300–400 μm thick (Fig. 10), which is comparable to the spatial resolution of the MR images. It is therefore likely that pixels in both the CBWM and CBGM ROIs contained contributions from the CBGr, and this may explain why the cerebellar ROIs had similar α_{MD}s.

Fig. 10 also contains images of the tissue in the corpus callosum and visual cortex. It is immediately evident that the distribution of nuclei in both of these areas is quite sparse in comparison to the CBGr, and the nuclei in the VC are much larger in diameter than those in any of the other ROIs (Table 3). The results of conventional PGSE or PGStE DTI have long been used to infer the geometry of these tissues. For example, it has been conjectured from conventional DTI that tissue in the CC has an elongated structure that is predominantly oriented along the principal axis of the ADT. Histology of the corpus callosum is consistent with this picture. The OGSE DTI results also do not contradict the presumption of an elongated geometry and in fact hint that more subtle structural information may be available. This assertion is supported by a recent application of the OGSE sequence to ex vivo rat spinal cord (Xu et al., 2012). With the MPG applied perpendicular to the primary fibre direction, it was found that the rate of change of the apparent diffusion coefficient (ADC) with frequency is linearly correlated with the mean axon diameter in different white matter tracts. It is possible that high spatial resolution OGSE DTI might be used as a noninvasive method to measure the mean axon diameter of fibre bundles in the CC and other white matter tissues.

In a similar way, conventional DTI implies that tissue in the VC is fairly homogeneous because the EVs have similar magnitudes and the FA is relatively low. However, with reference to the water sample, which is homogeneous and where all of the EVs and the FA accordingly show no dependence on frequency (Fig. 1), the OGSE DTI results correctly indicate that the tissue must in fact be inhomogeneous. It is difficult to identify from the type of stain used for Fig. 10 what part of the tissue may be directly responsible for the changes to the ADT, but it is well known that the visual cortex of both rodents and humans has a stratified cellular structure and a large number of nerve fibres running radially towards the cortical surface (e.g. Demyanenko et al., 2004; Leuze et al., 2012). The larger volume of cortical nuclei is another factor that may contribute.

As already noted in the Introduction, the only other complete application of OGSE to DTI was a small study performed on the cerebrum of an ex vivo monkey brain (Xu et al., 2010). Unfortunately, the results have not yet been published in full, but it is known that the FA was found to vary approximately linearly over the range 50–300 Hz. For a white matter ROI the FA decreased at a rate of about 0.8 kHz^{-1}, while the FA was relatively unaffected by MPG frequency for a grey matter ROI.

Finally, even though the full ADT was not measured, Does et al. (2003) did apply the OGSE sequence to estimate the MD of in vivo rat brain over the frequency range 38.5–500 Hz. The MD was found to increase substantially with increasing frequency, however, a solid comparison with the present data is hindered by the fact that the only measurements within the range 33.3–133.3 Hz were at 38.5 and 115.4 Hz. Nevertheless, if it is assumed that the MD is approximately linear in that range, a crude estimate from Fig. 8 of (Does et al., 2003) finds that the slope in normal cortical grey matter is around

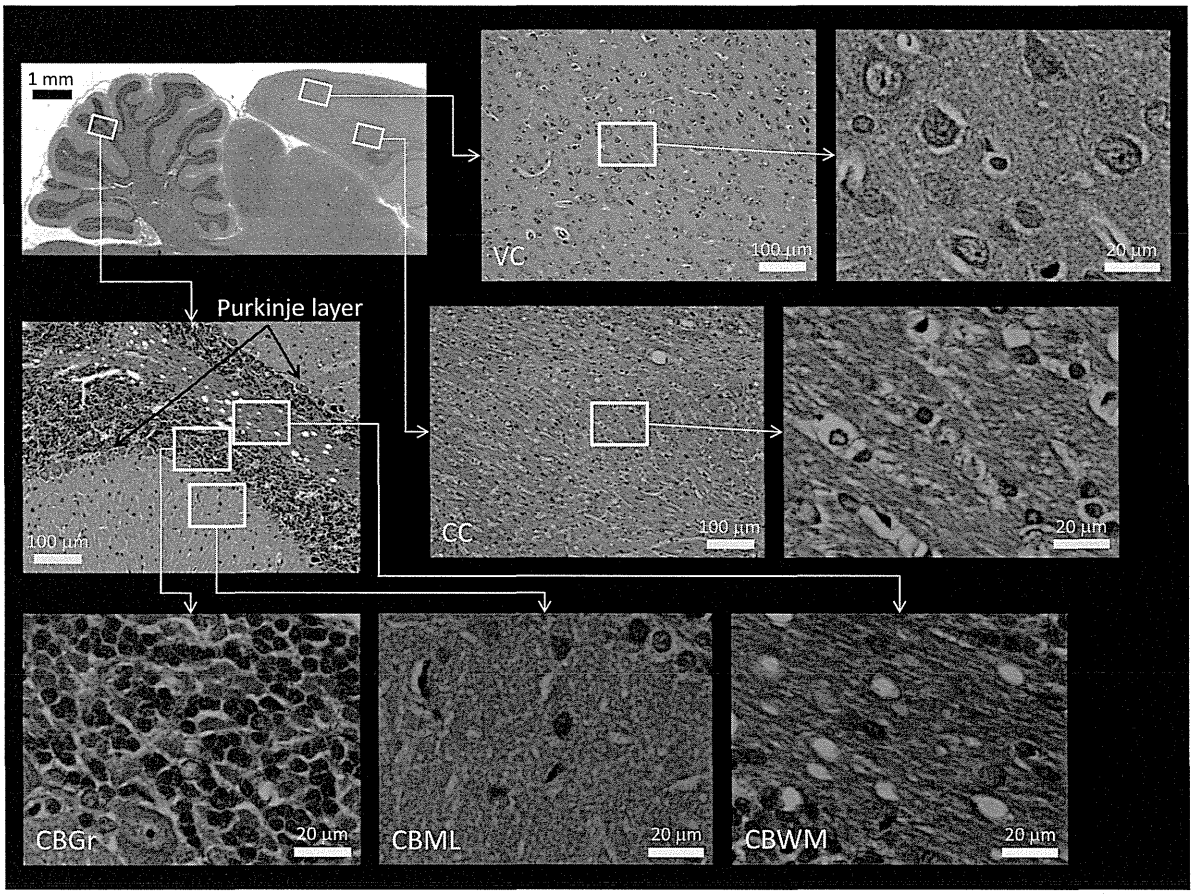

Fig. 10. Histology sections from an 8 week old rat in the same orientation as the imaging was performed. The tissue has been stained with haematoxylin and eosin, which stains cell nuclei blue or purple and the cytoplasm, connective tissue and other extracellular substances various shades of pink or red. The yellow rectangles on the figure in the upper left corner show the locations of the higher magnification images pointed to by the arrows, and this pattern is repeated for the rectangles in the next level of images. A scale bar is also shown on each image. Each of the higher magnification images zooms in on an area within the ROIs studied in the manuscript. Note that, rather than just CBWM and CBGM images, the cerebellum has been classified into three tissue categories: the CBWM, cerebellar granule cell layer (CBGr) and cerebellar molecular layer (CBML).

$0.36\mu m^2$, which is compatible with the MD estimate found here for the VC ROI.

On the changes to the MD and FA with frequency

From the results in Figs. 6 and 7 it is immediately clear why the MD behaves as it does in Figs. 3 and 4a. Denoting the ith EV at frequency f by λ_i, over the range of frequencies used it was found that

$$\lambda_i \simeq \alpha_{\lambda_i} f + \beta_{\lambda_i}, \tag{1}$$

which means that $dMD/df \simeq \alpha_{\lambda_1} + \alpha_{\lambda_2} + \alpha_{\lambda_3}$. It follows that the MDs of the CBWM, CBGM and VC increase strongly with MPG frequency because all of the EVs do, while the increase in MD of the CC is less dramatic because only the largest EV increases substantially with frequency.

Table 3
Characteristics of the nuclei in the highest magnification images of Fig. 10.

Tissue	Nuclear diameter (μ m)	# Nuclei	% of total area
CBWM	8–10	16	7–12
CBGr	4–6	205	23–52
CBML	6–8	10	3–5
VC	12–14	16	16–23
CC	4–6	22	2–6

An explanation for the behaviour of the FA (Figs. 4b and 5) is a little more complicated. First note that even though the FA is defined as a nonlinear function of all three EVs ($\lambda_1 \geq \lambda_2 \geq \lambda_3 \geq 0$) (Basser and Pierpaoli, 1996), by making the change of variables $(\mu_1,\mu_2) = (\lambda_2/\lambda_1, \lambda_3/\lambda_2)$ it can be rewritten as a function of only two independent variables

$$FA(\mu_1,\mu_2) = \sqrt{\frac{(1-\mu_1)^2 + (1-\mu_1\mu_2)^2 + \mu_1^2(1-\mu_2)^2}{2\left[1+\mu_1^2(1+\mu_2^2)\right]}} \tag{2}$$

with domain $[0,1]\times[0,1]$. The advantage of this form is that the reduced number and finite range of the independent variables allows the changes to the FA and EVs to be simultaneously visualised on a contour plot like that shown in Fig. 11. At any point $\boldsymbol{\mu}$ on the plot

$$\frac{dFA}{df} = \partial_{\mu_1} FA\left[\frac{d\mu_1}{df} + \kappa\frac{d\mu_2}{df}\right], \tag{3}$$

where $\kappa = \partial_{\mu_2} FA/\partial_{\mu_1} FA$ has been defined. A quick glance at the figure establishes that $\partial_{\mu_1} FA < 0$ and $\partial_{\mu_2} FA \leq 0$ throughout the domain, and therefore it is always true that $\kappa \geq 0$. After using Eq. (1), it is also easy to see that $d\mu_j/df \simeq \left(\alpha_{\lambda_{j+1}}\lambda_j - \alpha_{\lambda_j}\lambda_{j+1}\right)/\lambda_j^2$ is positive or negative depending on whether $\alpha_{\lambda_{j+1}}/\alpha_{\lambda_j}$ is greater or less, respectively, than λ_{j+1}/λ_j $(=\mu_j)$. For example, for the CBWM ROI the 1st and 2nd EVs increase strongly with frequency at about the same rate (Fig. 7), but because the value of λ_2 is substantially less than λ_1 (Fig. 6), an

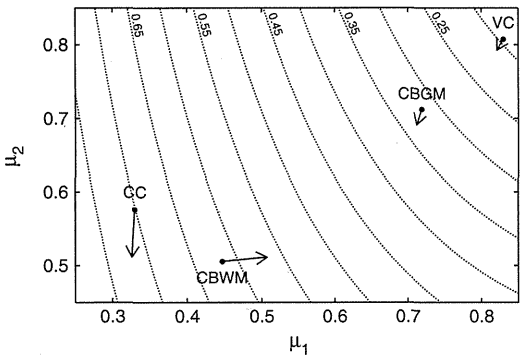

Fig. 11. Contour plot of $FA(\mu_1,\mu_2)$ as defined in Eq. (2). The horizontal and vertical axes correspond to μ_1 and μ_2, respectively, and the dotted contours represent lines of constant FA in steps of 0.05. Although the full domain of μ_1 and μ_2 is not shown in the figure, note that the point $\mu_1=\mu_2=1$ corresponds to $FA=0$ and from there the FA increases as either μ_1 or μ_2 decreases. Note also that the FA is always equal to 1 whenever $\mu_1=0$, and there are no local maxima, minima or saddle points within the domain. The positions of the closed circles correspond to the estimates of μ_1 and μ_2 at the lowest applied MPG frequency (33.3 Hz) for each of the in vivo ROIs. The solid line extending from each circle traces out the changes to the EVs and FA with increasing frequency before terminating with an arrowhead as the highest applied frequency (133.3 Hz) is reached. For the purposes of simplifying the figure, the uncertainty of the estimates has not been plotted.

increase in μ_1 with f results. Finally, knowing how these factors vary with frequency it can be understood from the figure that the FA decreases for the CBWM because both μ_1 and μ_2 increase with frequency. Similarly, the FA increases for the CBGM, CC and VC because μ_1 and μ_2 both decrease with frequency, although it should be remembered that the uncertainty analysis indicates that the changes to the FA are not significant or only minor for these ROIs (Figs. 4 and 5). In general, the FA may either increase or decrease depending on the size of the EVs relative to each other and also on the rates of change of the EVs with frequency.

Extracting quantitative morphological information: restricted diffusion and asymptotic diffusion-time behaviour

The results of this study demonstrate that OGSE DTI provides a qualitative advantage over conventional DTI because changes to the ADT have been observed in in vivo experiments. However, an important question remaining for OGSE DTI studies is how can this additional information be used to quantify the structure or condition of brain tissue? A potential means to extract quantitative information is to interpret the data within the mathematical framework developed for restricted diffusion.

The study of restricted diffusion with NMR has a long history stretching from the 1960s until the present (Grebenkov, 2007). In that time many theoretical studies have addressed the *forward problem* of calculating how a known geometry influences molecular diffusion and the corresponding signal attenuation (e.g. Tanner, 1978; Sukstanskii et al., 2004). In the theory, the physical problem of calculating the signal can be reduced to the mathematical problem of analysing the spectral properties of the Laplacian in the given geometry. As the eigenmodes are directly related to the shape of the confining medium, there is a great deal of information about the geometry encoded in the signal. It is therefore the *inverse problem* of what and how morphological information can be inferred from the observed signal that is more relevant to practical applications. One way to address this problem is to solve the forward problem for a model system and then fit the observed signal to the model to quantify the parameters defining the geometry. Although this strategy is used to some degree for successful fibre-tracking in white matter (e.g. CHARMED Assaf et al., 2004; AxCaliber Assaf et al., 2008) and estimating the dimensions of packed cell preparations (e.g. Xu et al., 2011), it has the obvious weakness of requiring some prior knowledge of the medium's geometry and the way the diffusing molecules interact with the microstructure. Moreover, it may be very difficult to describe the geometry of a complex medium with a manageable set of length parameters and some essential features of the system may be missing. In disordered media it is likely that the microstructure involves a wide range of length scales so that even the forward problem becomes formidable. It would be beneficial if a model-independent approach were available to characterise media with complicated internal architectures.

Perhaps the most extensive application of the concepts of restricted diffusion is the study of porous media (Sen, 2004). In materials of this type, diffusion-time dependent changes to the signal are often interpreted in terms of the asymptotic short- and long-time behaviour of the ADC. To be specific, in the limit of short diffusion-time (denoted by τ) it has been shown that the ADC approaches the free-diffusion value as $\sqrt{\tau}$, with the constant of proportionality related to the surface-to-pore-volume ratio of the medium (Mitra et al., 1992, 1993). At long diffusion-times the ADC is said to reach a constant value that is equal to the free-diffusion coefficient reduced by a geometrical factor called the tortuosity of the medium (Latour et al., 1994, 1995). Furthermore, this limiting value is approached as $1/\tau$, but, unlike the case for short τ, the geometrical meaning of the constant of proportionality is not universal as it depends on the details of the system at hand (Sen, 2003; de Swiet and Sen, 1996). Neither of these limits provides specific details of the pore geometry, but the coefficients estimated from the asymptotic τ behaviour of the data can be used to characterise the medium in a geometrical sense.

While the behaviour of water in living tissue is more complicated than that in an inanimate porous medium, it is thought that many of the concepts of restricted diffusion can also be applied to biological systems (Helmer et al., 1995; Sen, 2003). The strongest evidence for restriction effects in vivo is nonexponential signal attenuation at high b-values (e.g. Assaf and Cohen, 1998; Pfeuffer et al., 1999) and modulation of image contrast with MPG orientation (e.g. Moseley et al., 1990; Doran et al., 1990). Other studies have argued that differences in the signal attenuation for the same high b-value and a range of very long diffusion-times, indicate water exchange between spatial compartments separated by barriers that hinder molecular motion (e.g. Pfeuffer et al., 1999; Clark and Le Bihan, 2000; Meier et al., 2003). In fact, most of the changes needed to adapt the theory of restricted diffusion to biological investigations can be achieved by altering the boundary conditions to accommodate membrane permeability. One model following this approach found that even after doing so, the short-time behaviour of the ADC is unaffected from the case for porous media (Sen, 2003). That is, inclusion of the permeability only alters the coefficients of terms with linear or higher order dependence on τ. In contrast, it has been suggested that the ADC asymptotically approaches its long-time limit as $1/\sqrt{\tau}$ rather than $1/\tau$ when membrane permeability is accounted for (Sen, 2004). In this case the expansion coefficient depends on the permeability as well as pure geometry effects (Latour et al., 1994).

One way that the results presented in this manuscript can be considered in the context of restricted diffusion is to make use of the improvised effective diffusion-time (Does et al., 2003; Gross and Kosfeld, 1969; Parsons et al., 2003). Even if the effective diffusion-time is only valid over a limited range of frequencies (Novikov and Kiselev, 2011), it is assumed that it can be used in this case because the spectrum of applied frequencies (33.3–133.3 Hz) is relatively narrow. Replacing f by $1/4\tau$ in Eq. (1), it is immediately apparent that those EVs of the ADT having a significant dependence on MPG frequency correspondingly have a $1/\tau$ dependence on diffusion-time, fulfilling the hopes for the OGSE sequence expressed near the end of the Introduction. To illustrate the point further, the EVs of the CBWM ROI (normalised by the diffusion coefficient of free water at 37°C (Goodman et al., 2005)) have been replotted as a function of τ in Fig. 12. Also, after inserting the estimates of α_{λ_i} and β_{λ_i} for the

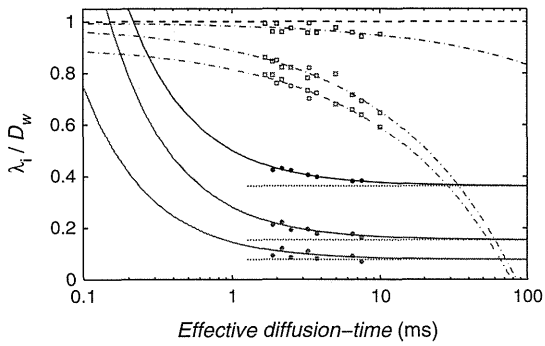

Fig. 12. The EVs of the CBWM ROI (closed circles) normalised by the diffusion coefficient of free water at 37 °C ($D_w \approx 3\mu m^2/ms$) have been plotted against the effective diffusion-time. The solid lines are fits to the data with Eq. (1) and $f = 1/4\tau$, while the horizontal dotted lines represent the predicted asymptotic limit as τ approaches ∞. Similar behaviour was also found for the other rat ROIs. These curves suggest that the rat data was acquired near to the long diffusion-time limit. For comparison, the EVs of the asparagus data (open squares) normalised by the diffusion coefficient of water at 22 °C ($D_w \approx 2\mu m^2/ms$) are also plotted. The dashed lines are reasonable fits to the data as a linear function of $\sqrt{\tau}$, and suggest that the asparagus data might have been acquired in the short diffusion-time limit for this sample.

CBWM EVs into Eq. (1), curves extrapolating the behaviour of the EVs to the range 0.1–100 ms have been drawn on the figure. For diffusion-times above 10–20 ms the figure predicts that the EVs approach a constant value, while for the range below 1 ms the curves forecast that the EVs increase towards the free-diffusion limit as the diffusion-time decreases. Although not shown, similar trends were also found for the other rat ROIs. These results suggest that the rat data was acquired near to the long diffusion-time limit. For comparison, the asparagus EVs (normalised by the diffusion coefficient of water at 22 °C) have also been replotted as a function of τ on Fig. 12. It is evident that the asparagus data does not behave as either $1/\tau$ or $1/\sqrt{\tau}$. However, after noting that the largest asparagus EV is very close to the free-diffusion limit, a fit to $\sqrt{\tau}$ was performed for each EV. From inspection the fit seems to be in good agreement with the data over the range of available diffusion-times. It is therefore possible to deduce that the asparagus data is compatible with the short diffusion-time limit.

Even though Fig. 12 suggests that the rat and asparagus data may be interpreted in the long and short diffusion-time limits, respectively, it does not automatically follow that the parameters estimated from the fits with respect to τ correspond to the coefficients associated with the asymptotic behaviour of the ADC discussed above. The short and long diffusion-time asymptotics predicted by the theory were constructed under the assumption of statistical isotropy at macroscopic length scales, for which case the diffusion behaviour can be described by a scalar function of τ. To the best of the authors' knowledge, an extension of the asymptotic theory to media with macroscopic anisotropy has not been previously considered in the restricted diffusion literature. Without providing a rigorous derivation, it is possible to consider that issue here. First of all, the short-time limit of the ADT must be the same as it is for the scalar case: the diffusion coefficient of free water. However, rather than the ADT collapsing to a scalar before reaching the limit, it seems more likely that each EV of the ADT independently approaches the limit as $\sqrt{\tau}$ at its own rate. Therefore, a possible generalisation of the surface-to-volume ratio is to a tensor quantity that reflects the fact that the nett surface area obstructing molecular motion normal to the orientation of the applied MPG will vary if the medium possesses long-range order in any particular direction. It follows that the coefficients of $\sqrt{\tau}$ calculated from the asparagus data are the EVs of this tensor for that vegetable.

The situation for the long-time limit of the ADT must be similar. That is, rather than using a scalar coefficient depending on the permeability and tortuousity, an extension to a tensor quantity is necessary to describe the results. In this case the physical meaning of the tensor is not immediately clear, but could reflect the fact that the path length between interactions with the obstructing surfaces will on average be longer in certain directions when the tissue is anisotropic at the macroscopic scale. In this case the estimates of the α_{λ_i} from the rat data would correspond to the EVs of that tensor.

Conclusion

OGSE DTI has been applied to in vivo rat brain and clear frequency-dependent alterations to the ADT were observed in all four of the ROIs selected for detailed analysis. The dependence on frequency was approximately linear over the range 33.3–133.3 Hz. All ROIs showed clear increases in MD. While CBWM was the only ROI to show a substantial decrease in FA, the CC and VC had minor increases of the same parameter. All EVs of the ADT tended to increase with MPG frequency in the CBWM, CBGM and VC ROIs, but only the principal EV was found to increase significantly for the CC. Whereas the behaviour of the MD has a simple relationship to the frequency-dependence of the EVs, the relationship between the FA and the EVs with frequency can be most easily understood by redefining the FA to be a function of only two independent variables. It was shown that the FA may either increase or decrease depending on the size of the EVs relative to each other and also on the rates of change of the EVs with frequency. There was no evidence that the orientation of the principal eigenvector of the ADT varied systematically with frequency. Pixelwise linear fits to the MD from individual animals found elevated changes across the cerebellum, suggesting that there may be a contrast in the brains of live animals similar to that discovered in ex vivo brain tissue. It is also worth noting that the ADT was not significantly altered by MPG frequency in a pure water sample, but clear changes were observed due to the presence of microstructure in an asparagus sample. Finally, it is not yet fully understood how the changes to the ADT might be utilised to extract quantitative information about tissue microstructure. A possible interpretation in terms of restricted diffusion and the asymptotic time behaviour of the ADT was discussed, and it was suggested that the asparagus and rat data correspond to the short and long diffusion-time limits, respectively. Histology confirmed that the tissue in each of the ROIs had a different microstructure and therefore the coefficients estimated from the asymptotic diffusion-time behaviour might be used to classify different tissues.

Supplementary data to this article can be found online at http://dx.doi.org/10.1016/j.neuroimage.2012.12.036.

Acknowledgments

The authors would like to thank Sayaka Shibata and Chinami Kajiwara for their assistance with animal care, and Teppei Nakahara and Daisuke Kokuryo for their technical assistance. Thanks are also extended to Professor Kazuhiko Sawada of the Tsukuba International University for helpful discussions. This research was supported by a Grant-in-Aid for Scientific Research (Kakenhi) from the Japan Society for the Promotion of Science (JSPS). It was also partially supported by the JSPS through its "Funding Program for World-Leading Innovative R&D on Science and Technology (FIRST Program)."

References

Aggarwal, M., Jones, M.V., Calabresi, P.A., Mori, S., Zhang, J., 2012. Probing mouse brain microstructure using oscillating gradient diffusion MRI. Magn. Reson. Med. 67, 98–109.

Assaf, Y., Cohen, Y., 1998. Non-mono-exponential attenuation of water and N-acetyl aspartate signals due to diffusion in brain tissue. J. Magn. Reson. 131, 69–85.

Assaf, Y., Freidlin, R.Z., Rohde, G.K., Basser, P.J., 2004. New modeling and experimental framework to characterize hindered and restricted water diffusion in brain white matter. Magn. Reson. Med. 52, 965–978.

Assaf, Y., Blumenfeld-Katzir, T., Yovel, Y., Basser, P.J., 2008. AxCaliber: a method for measuring axon diameter distribution from diffusion MRI. Magn. Reson. Med. 59, 1347–1354.
Basser, P.J., Pierpaoli, C., 1996. Microstructural and physiological features of tissues elucidated by quantitative-diffusion-tensor MRI. J. Magn. Reson. B 111, 209–219.
Basser, P.J., Mattiello, J., Le Bihan, D., 1994. MR diffusion tensor spectroscopy and imaging. Biophys. J. 66, 259–267.
Clark, C.A., Le Bihan, D., 2000. Water diffusion compartmentation and anisotropy at high b values in the human brain. Magn. Reson. Med. 44, 852–859.
Clark, C.A., Hedehus, M., Moseley, M., 2001. Diffusion time dependence of the apparent diffusion tensor in healthy human brain and white matter disease. Magn. Reson. Med. 45, 1126–1129.
Colvin, D.C., Yankeelov, T.E., Does, M.D., Yue, Z., Quarles, C., Gore, J.C., 2008. New insights into tumor microstructure using temporal diffusion spectroscopy. Cancer Res. 68, 5941–5947.
Colvin, D.C., Jourquin, J., Xu, J., Does, M.D., Estrada, L., Gore, J.C., 2011. Effects of intracellular organelles on the apparent diffusion coefficient of water molecules in cultured human embryonic kidney cells. Magn. Reson. Med. 65, 796–801.
de Swiet, T.M., Sen, P.N., 1996. Time-dependent diffusion coefficient in a disordered medium. J. Chem. Phys. 104, 206–209.
Demyanenko, G.P., Schachner, M., Anton, E., Schmid, R., Feng, G., Sanes, J., Maness, P.F., 2004. Close homolog of L1 modulates area-specific neuronal positioning and dendrite orientation in the cerebral cortex. Neuron 44, 423–437.
Does, M.D., Parsons, E.C., Gore, J.C., 2003. Oscillating gradient measurements of water diffusion in normal and globally ischemic rat brain. Magn. Reson. Med. 49, 206–215.
Doran, M., Hajnal, J.V., Van Bruggen, N., King, M.D., Young, I.R., Bydder, G.M., 1990. Normal and abnormal white matter tracts shown by MR imaging using directional diffusion weighted sequences. J. Comput. Assist. Tomogr. 14, 865–873.
Efron, B., Tibshirani, R.J., 1994. An Introduction to the Bootstrap. Chapman & Hall/CRC.
Goodman, J.A., Kroenke, C.D., Bretthorst, G.L., Ackerman, J.J.H., Neil, J.J., 2005. Sodium ion apparent diffusion coefficient in living rat brain. Magn. Reson. Med. 53, 1040–1045.
Grebenkov, D.S., 2007. NMR survey of reflected Brownian motion. Rev. Mod. Phys. 79, 1077–1137.
Gross, B., Kosfeld, R., 1969. Anendung der Spin-Echo-Methode der Messung der Selbstdiffusion. Messtechnik 77, 171–177.
Helmer, K.G., Dardzinski, B.J., Sotak, C.H., 1995. The application of porous-media theory to the investigation of time-dependent diffusion in in vivo systems. NMR Biomed. 8, 297–306.
Horsfield, M.A., Lai, M., Webb, S.L., Baker, G.J., Tofts, P.S., Turner, R., Rudge, P., Miller, D.H., 1996. Apparent diffusion coefficients in benign and secondary progressive multiple sclerosis by nuclear magnetic resonance. Magn. Reson. Med. 36, 393–400.
Kershaw, J., Leuze, C., Autio, J., Shibata, S., Obata, T., Kanno, I., Aoki, I., 2010. Apparent diffusion anisotropy in rat cerebellum is altered at short effective diffusion-times using oscillating-gradient diffusion-tensor MRI. Proceedings of the Joint EUROMAR 2010 and 17th ISMAR Conference, p. 296.
Kershaw, J., Leuze, C., Obata, T., Kanno, I., Aoki, I., 2011. Changes to the fractional anisotropy and mean diffusivity of in vivo rat brain measured at short effective diffusion times. Proceedings of the 19th Annual Meeting of ISMRM, 409.
Latour, L.L., Svoboda, K., Mitra, P.P., Sotak, C.H., 1994. Time-dependent diffusion of water in a biological model system. Proc. Natl. Acad. Sci. U. S. A. 91, 1229–1233.
Latour, L.L., Kleinberg, R.L., Mitra, P.P., Sotak, C.H., 1995. Pore-size distributions and tortuosity in heterogeneous porous media. J. Magn. Reson. 112, 83–91.
Le Bihan, D., Turner, R., Douek, P., 1993. Is water diffusion restricted in human brain white matter? An echo-planar imaging study. Neuroreport 4, 887–890.
Leuze, C.W.U., Anwander, A., Bazin, P.-L., Dhital, B., Stüber, C., Reimann, K., Geyer, S., Turner, R., 2012. Layer-specific intracortical connectivity revealed with diffusion MRI. Cereb. Cortex http://dx.doi.org/10.1093/cercor/bhs311.
Mardia, K.V., Jupp, P.E., 2000. Directional Statistics. Wiley.
Meier, C., Dreher, W., Leibfritz, D., 2003. Diffusion in compartmental systems. II. Diffusion-weighted measurements of rat brain tissue in vivo and postmortem at very large b-values. Magn. Reson. Med. 50, 510–514.
Mitra, P.P., Sen, P.N., Schwartz, L.M., Le Doussal, P., 1992. Diffusion propagator as a probe of the structure of porous media. Phys. Rev. Lett. 24, 3555–3558.
Mitra, P.P., Sen, P.N., Schwartz, L.M., 1993. Short-time behaviour of the diffusion coefficient as geometrical probe of porous media. Phys. Rev. B 47, 8565–8574.
Moonen, C.T.W., Pekar, J., de Vleeschouwer, M.H.M., van Gelderen, P., van Zijl, P.C.M., DesPres, D., 1991. Restricted and anisotropic displacement of water in healthy cat brain and in stroke studied by NMR diffusion imaging. Magn. Reson. Med. 19, 327–332.
Moseley, M., Cohen, Y., Kucharczyk, J., Mintorovitch, J., Asgari, H.S., Wendland, M.F., Tsuruda, J., Norman, D., 1990. Diffusion-weighted MR imaging of anisotropic water diffusion in cat central nervous system. Radiology 176, 439–445.
Niendorf, T., Norris, D.G., Leibfritz, D., 1994. Detection of apparent restricted diffusion in healthy rat brain at short diffusion times. Magn. Reson. Med. 32, 672–677.
Niendorf, T., Dijkhuizen, R.M., Norris, D.G., van Lookeren Campagne, M., Nicolay, K., 1996. Biexponential attenuation in various states of brain tissue: implications for diffusion-weighted imaging. Magn. Reson. Med. 36, 847–857.
Novikov, D.S., Kiselev, V.G., 2011. Surface-to-volume ratio with oscillating gradients. J. Magn. Reson. 210, 141–145.
Parsons, E.C., Does, M.D., Gore, J.C., 2003. Modified oscillating gradient pulses for direct sampling of the diffusion spectrum suitable for imaging sequences. Magn. Reson. Imaging 21, 279–285.
Parsons, E.C., Does, M.D., Gore, J.C., 2006. Temporal diffusion spectroscopy: theory and implementation in restricted systems using oscillating gradients. Magn. Reson. Med. 55, 75–84.
Pfeuffer, J., Provencher, S.W., Gruetter, R., 1999. Water diffusion in rat brain in vivo as detected at very large *b* values is multicompartmental. MAGMA 8, 98–108.
Pilatus, U., Shim, H., Artemov, D., Davis, D., van Zijl, P.C.M., Glickson, J.D., 1997. Intracellular volume and apparent diffusion constants of perfused cancer cell cultures, as measured by NMR. Magn. Reson. Med. 37, 825–832.
Schachter, M., Does, M.D., Anderson, A.W., Gore, J.C., 2000. Measurement of restricted diffusion using an oscillating gradient spin-echo sequence. J. Magn. Reson. 147, 232–237.
Schwartzman, A., Dougherty, R.F., Taylor, J.E., 2005. Cross-subject comparison of principal diffusion direction maps. Magn. Reson. Med. 53, 1423–1431.
Sen, P.N., 2003. Time-dependent diffusion coefficient as a probe of the permeability of the pore wall. J. Chem. Phys. 119, 9871–9876 (erratum 120, 11965–11966).
Sen, P.N., 2004. Time-dependent diffusion coefficient as a probe of geometry. Concepts Magn. Reson. 23A, 1–21.
Sukstanskii, A.L., yablonskiy, D.A., Ackerman, J.J.H., 2004. Effects of permeable boundaries on the diffusion-attenuated MR signal: insights from a one-dimensional model. J. Magn. Reson. 170, 56–66.
Tanner, J.E., 1978. Transient diffusion in a system partitioned by permeable barriers. Application to NMR measurements with a pulsed field gradient. J. Chem. Phys. 69, 1748–1754.
Tuch, D.S., 2004. Q-ball imaging. Magn. Reson. Med. 52, 1358–1372.
Tuch, D.S., Reese, T.G., Wiegell, M.R., Makris, N., Belliveau, J.W., Wedeen, V.J., 2002. High angular resolution diffusion imaging reveals intravoxel white matter fiber heterogeneity. Magn. Reson. Med. 48, 577–582.
van Gelderen, P., de Vleeschouwer, M.H.M., DesPres, D., Pekar, J., van Zijl, P.C.M., Moonen, C.T.W., 1994. Water diffusion and acute stroke. Magn. Reson. Med. 31, 154–163.
Xu, J., Does, M.D., Gore, J.C., 2009. Sensitivity of MR diffusion measurements to variations in intracellular structure: effects of nuclear size. Magn. Reson. Med. 61, 828–833.
Xu, J., Jeong, H.-K., Does, M.D., Anderson, A.W., Chen, L., Gore, J.C., 2010. Dependence of fractional anisotropy on diffusion time: a frequency-domain analysis using temporal diffusion spectroscopy. Proceedings of the 18th Annual Meeting of ISMRM, 4038.
Xu, J., Xie, J., Jourquin, J., Colvin, D.C., Does, M.D., Quaranta, V., Gore, J.C., 2011. Influence of cell cycle phase on apparent diffusion coefficient in synchronized cells detected using temporal diffusion spectroscopy. Magn. Reson. Med. 65, 920–926.
Xu, J., Harkins, K.D., Horch, R.A., Does, M.D., Gore, J.C., 2012. Dependence of temporal diffusion spectroscopy on axon size in white matter tracts of rat spinal cord. Proceedings of the 20th Annual Meeting of ISMRM, 351.

DOI: 10.3727/096368912X657882

CT-0924 Accepted 09/30/2012 for publication in "*Cell Transplantation*"

Interferon-β delivery via human neural stem cell abates glial scar formation in spinal cord injury

Running title: Human neural stem cells in spinal cord injury

Yusuke Nishimura[1], Atsushi Natsume[1]*, Motokazu Ito[1], Masahito Hara[1], Kazuya Motomura[1], Ryuichi Fukuyama[2], Naoyuki Sumiyoshi[2], Ichio Aoki[3], Tsuneo Saga[3], Hong J. Lee[4], Toshihiko Wakabayashi[1] and Seung U. Kim[4,5]*

[1]Department of Neurosurgery, Nagoya University, Nagoya, Japan; [2]Division of Pathology, Konan Kosei Hospital, Aichi, Japan; [3]MR Molecular Imaging Team, Molecular Imaging Center, National Institute of Radiological Sciences, Chiba, Japan; [4]Medical Research Institute, Chung-Ang University College of Medicine, Seoul, Korea; [5]Division of Neurology, Department of Medicine, UBC Hospital, University of British Columbia, Vancouver, Canada

*Correspondence to:
Atsushi Natsume, MD, PhD
Department of Neurosurgery, Nagoya University School of Medicine
Nagoya 466-8550, Japan
Tel: 81-52-744-2353; Fax: 81-52-744-2360; E-mail: anatsume@med.nagoya-u.ac.jp
or
Seung U. Kim, MD, PhD
Division of Neurology, Department of Medicine, UBC Hospital, University of British Columbia
Vancouver, BC V6T 2B5, Canada
Tel: 82-2-820-5652; Fax: 82-2-813-5387; E-mail: sukim2005@gmail.com

Abstract

Glial scar formation is the major impedence to axonal regrowth after spinal cord injury (SCI), and scar-modulating treatments have become a leading therapeutic goal for SCI treatment. In this study human neural stem cells (NSCs) encoding interferon (IFN)-β gene were administered

intravenously to mice 1 week after spinal cord injury. Animals receiving NSCs encoding IFN-β exhibited significant neurobehavioral improvement, electrophysiological recovery, suppressed glial scar formation and preservation of nerve fibers in lesioned spinal cord. Systemic evaluation of SCI gliosis lesion site with lesion-specific microdissection, genome-wide microarray and MetaCore pathway analysis identified upregulation of toll-like receptor (TLR)-4 in SCI gliosis lesion site, and this led us to focus on TLR-4 signaling in reactive astrocytes. Examination of primary astrocytes from TLR-4 knockout mice, and in vivo inhibition of TLR-4, revealed that the effect of IFN-β on the suppression of glial scar formation in SCI requires TLR-4 stimulation. These results suggest that IFN-β delivery via intravenous injection of NSCs following SCI inhibits glial scar formation in spinal cord through stimulation of TLR-4 signaling.

Introduction

Spinal cord injury (SCI) is a devastating clinical condition that results in permanent disability due to very limited regenerative capability of the adult human spinal cord. One major impediment to axonal regeneration in SCI is glial scar formation, a process mainly directed by reactive astrocytes (42). Normally, quiescent astrocytes in adults respond vigorously to injury; during the acute phase of injury, some of these responses have beneficial effects, such as isolating the injury site and minimizing the area of inflammation and cellular degeneration. Some astrocyte populations may even support axonal regrowth (6); however, astrocytes eventually become hypertrophied and proliferative, upregulate the expression of glial fibrillary acidic protein (GFAP), and form a dense network of glial processes around the

injury site (12). Therefore, scar-modulating treatments have become a leading therapeutic goal for the treatment of SCI (9,37).

We have previously examined the ability of liposome-mediated IFN-β gene delivery to inhibit the formation of glial scar tissue in a SCI mouse model (12) and found that the IFN-β administration induced functional and structural recovery in injured spinal cord including regrowth of corticospinal tract (CST) axons.

Recently, there has been a great deal of interest in the potential use of stem cells in SCI treatment because of their abilities to self-renew, migrate, and differentiate into all types of neural cells (18). Neural stem cells (NSCs), in particular, are characterized by the capability to home in and deliver therapeutic genes (40), and constitute a promising source for cell replacement therapy (22,25,45).

In the present study, we attempted to attain neuronal regrowth via intravenous transplantation of human NSCs encoding genes for cytosine deaminase (CD) and IFN-β (F3.CD.IFN). We investigated whether human NSCs transduced with IFN-β gene can inhibit glial scar formation and improve spinal function after SCI, while the CD gene, a therapeutic suicide gene that converts non-toxic prodrug 5-fluorocytosine (5-FC) into toxic 5-fluorouracil (5-FU), provides a safe guard to allow removal of cells in cases of undesirable proliferation..

Further, in order to clarify the function of IFN-β, we attempted to identify profile changes in SCI gliosis lesion site by using gliosis site-specific microdissection, genome-wide microarray, and MetaCore pathway analysis. This systematic data processing revealed the upregulation of toll-like receptor (TLR)-4, and we subsequently focused on the functional role of TLR-4 signaling cascades in reactive astrocytes. We here verify that the SCI-induced proliferation of reactive astrocytes in lesion is suppressed by the ligation of TLR-4 in the presence of IFN-β.

Materials and methods

Neural stem cells

The HB1.F3 (F3) human NSC line was generated from human fetal telencephalon and immortalized by transfection with a retroviral vector encoding the v-myc oncogene, as described previously(21). It has been confirmed that this human NSC line is capable of self-renewal and has multipotent capacity to differentiate into neuronal or glial cell lineages both in vivo and in vitro(21). The F3 cell line was infected with a replication-incompetent retroviral vector encoding β-galactosidase (lacZ) and puromycin-resistance genes. The cell line was subsequently designated as F3.LacZ. In this study, the clonal F3.CD.IFN-β line (F3.CD.IFN) was derived from parental F3.CD cells, as previously described(1,11). F3.LacZ and F3.CD.IFN cells were cultured in Dulbecco's modified Eagle's medium (DMEM) with high glucose (Invitrogen, Carlsbad,
CA) supplemented with 10% fetal bovine serum (FBS), 100 U/mL penicillin, and 100 μg/mL streptomycin.

In vitro assay of astrocyte suppression by F3.CD.IFN cells

The suppressive effects of F3.LacZ and F3.CD.IFN cells on the growth of primary-cultured astrocytes were quantified in the presence or absence of 5-FC (Sigma-Aldrich, St. Louis, MO). Primary astrocyte cultures were prepared from the cerebral hemispheres of fetal BALB-c nude mice (SLC, Shizuoka, Japan). The hemispheres were cleared of the meninges and choroid plexus and digested with 0.1% trypsin (Invitrogen) in phosphate-buffered saline (PBS) for 30 min at 37°C, followed by dissociation into single cells by repeated pipetting. A suspension containing 2×10^5 cells was seeded into 35-mm poly-L-lysine-coated Petri dishes, and the majority of cells
(90–95%) were confirmed to be astrocytes based on immunocytochemical analysis for GFAP expression. Astrocytes were cultured on Petri dishes for 1 week, after which F3.NSCs were

added to the astrocyte cultures. Astrocytes were co-cultured with either F3.LacZ or F3.CD.IFN at various ratios of astrocytes to F3 cells (1:0, 20:1, and 40:1). F3 cells were prelabeled by incubating for 20 min in culture medium containing the cell tracker CM-DiI (Invitrogen), which emits 570-nm fluorescence. For experiments using F3.CD.IFN cells treated with 5-FC, 5-FC was added to the conditioned medium at a final concentration of 500 mg/mL following 24 h of culture, and the culture was maintained for24 hr. Cells were subsequently immunostained with anti-GFAP antibody (DAKO, Glostrup, Denmark) and Alexa 488-labeled IgG (Molecular Probes, Eugene, OR). The cultures were analyzed using an Olympus FV5-PSU confocal laser microscope (Olympus, Tokyo, Japan), and the total numbers of GFAP-positive cells were counted. Each experiment was performed in triplicate. The suppressive effects of F3.LacZ and F3.CD.IFN on the growth of primary-cultured TLR-4 deficient astrocytes were also quantified. Primary TLR-4 deficient astrocyte cultures were prepared from the cerebral hemispheres of fetal TLR-4 knock- out mice (Oriental Bio, Kyoto Japan). A suspension containing 2 × 105 cells was seeded onto 35-mm poly-L-lysine-coated Petri dishes. The majority of cells (90–95%) were immunocytochemically confirmed to be astrocytes and cultured on Petri dishes for 1 week, after which F3.NSCs were added to the astrocyte cultures. Astrocytes were co-cultured with either F3.LacZ or F3.CD.IFN cells at various ratios of astrocytes to F3 cells (1:0, 20:1, and 40:1). F3 cells were prelabeled by the cell tracker CM-DiI, and the culture was maintained for 2 days. Cells were subsequently immunostained with anti-GFAP antibody followed by Alexa 488-labeled IgG, and the total numbers of GFAP-positive cells were counted. Each experiment was performed in triplicate.

Spinal transection procedure

Adult female Balb-c nude mice (8–12 weeks old; SLC) were used in this study. All experiments were performed in accordance with the ethical guidelines of the Nagoya University Institutional Animal Care and Use Committee. The mice were anesthetized with

1.5% halothane and maintained on 1.25% halothane in an oxygen-nitrous oxide gas mixture. Laminectomy was performed at vertebral level T9–T10. The dura was opened, and the dorsal half of the spinal cord was transected to a depth of 1 mm with a pair of extra-fine microscissors. In the sham group, laminectomy was conducted without the accompanying SCI. Following spinal transection, the overlying muscle and skin were sutured. The mice were placed on soft bedding on a warming blanket held at 37°C for 1 hr after surgery. One week later, the motor function of each animal was evaluated according to the Basso Mouse Scale (BMS), as described below. Only animals with BMS scores below 4 out of 9 points were used. These were divided randomly into 4 treatment groups: (1) PBS group, SCI with intravenous administration of 100 µL PBS;

(2) F3.LacZ group, SCI with intravenous administration of F3.LacZ (2 × 106 cells in 100 µL of PBS); (3) F3.CD.IFN group, SCI with intravenous administration of F3.CD.IFN (2 ×10^6 cells in 100 µL of PBS); and (4) F3.CD.IFN+5-FC group, SCI with intravenous administration of F3.CD. IFN (2 × 10^6 cells in 100 µL of PBS) and, beginning 2 days later, 10 intraperitoneal injections of 5-FC daily (900 mg/kg). In order to elucidate the mechanism by which IFN-β elicits effects following SCI, we used the same spinal transection procedure and assigned the mice to 2 treatment groups 1 week later: (1) F3.LacZ group, SCI with intravenous administration of F3.LacZ

(2 × 10^6 cells in 100 µL of PBS); (2) F3.CD.IFN group, SCI with intravenous administration of F3.CD.IFN (2 × 10^6 cells in 100 µL of PBS). In addition, the F3.CD.IFN group was randomly divided into 2 further groups 1 week after the initial group assignment: (2-a) F3.CD.IFN group, (2-b) F3.CD.IFN+OxPAPC group, SCI with intravenous administration of F3.CD.IFN (2 × 10^6 cells in 100 µL of PBS), and 7 days later, an intraperitoneal injection of 50 µg of OxPAPC (TLR4 Inhibitor; InvivoGen, San Diego, CA). Finally, we compared the functional recovery in F3.LacZ, F3.CD.IFN and F3.CD.IFN+OxPAPC groups.

Laser-captured microdissection and microarray